Oxygen self-supplying small size magnetic nanoenzymes for synergistic photodynamic and catalytic therapy of breast cancer†

Xinyi Cai,‡[a] Tiantian Xu,‡[b] Rui Ding,‡[a] Dou Zhang,[a] Guiquan Chen,[c] Wenchang Zhao,[a] Jiajie Hou,[e] Hong Pan, [ID] *[b] Qian Zhang*[d] and Ting Yin*[a]

In recent years, tumor catalytic therapy based on nanozymes has attracted widespread attention. However, its application is limited by the tumor hypoxic microenvironment (TME). In this study, we developed oxygen-supplying magnetic bead nanozymes that integrate hemoglobin and encapsulate the photosensitizer curcumin, demonstrating reactive oxygen species (ROS)-induced synergistic breast cancer therapy. Fe_3O_4 magnetic bead-mediated catalytic dynamic therapy (CDT) generates hydroxyl radicals ($^{\bullet}OH$) through the Fenton reaction in the tumor microenvironment. The Hb-encapsulated Fe_3O_4 magnetic beads can be co-loaded with the photosensitizer/chemotherapeutic agent curcumin (cur), resulting in Fe_3O_4-Hb@cur. Under hypoxic conditions, oxygen molecules are released from Fe_3O_4-Hb@cur to overcome the TME hypoxia, resulting in comprehensive effects favoring anti-tumor responses. Upon near-infrared (NIR) irradiation, Fe_3O_4-Hb@cur activates the surrounding molecular oxygen to generate a certain amount of singlet oxygen ($^1O_2$), which is utilized for photodynamic therapy (PDT) in cancer treatment. Meanwhile, we validated that the O_2 carried by Hb significantly enhances the intracellular ROS level, intensifying the catalytic therapy mediated by Fe_3O_4 magnetic beads and inflicting lethal damage to cancer cells, effectively inhibiting tumor growth. Therefore, significant *in vivo* synergistic therapeutic effects can be achieved through catalytic–photodynamic combination therapy.

1. Introduction

Nanocatalytic therapy is widely used in cancer treatment due to its enormous advantages such as high selectivity,[1] low toxicity,[2,3] high efficiency,[4–6] and tunability.[7] Efficient tumor catalysts, such as hydrogen peroxide enzymes, metal nanoparticles, and porphyrin compounds, can induce the generation of reactive oxygen species (ROS), including singlet oxygen ($^1O_2$), hydroxyl radicals ($^{\bullet}OH$), and superoxide anions ($^{\bullet}O^{2-}$).[8,9] By harnessing the power of these natural ROS, it is possible to effectively induce oxidative damage to cancer cells and shrink tumors, which has been adopted and further explored for *in vivo* tumor therapy.[10] Despite these significant advancements, there are still challenging factors that limit the potential efficacy of catalytic therapy.[11,12] One of the major challenges is the inherently hypoxic tumor microenvironment (TME) within solid tumors, which significantly restricts the effectiveness of nanocatalytic therapy in clinical applications.[13,14]

Chemodynamic therapy (CDT), which enhances intracellular ROS through the utilization of the Fenton reaction, has garnered significant attention in cancer treatment.[15,16] Considering the overexpression of hydrogen peroxide (H_2O_2) and mild acidic conditions in the TME, extensive exploration has been conducted on advanced nanocatalysts to capture H_2O_2 as a substrate.[17–19] However, achieving sufficient and satisfactory therapeutic efficacy remains challenging due to the limited endogenous oxygen (O_2) content.[20] Hemoglobin (Hb) is a composite protein composed of four subunits. Each Hb molecule consists of two α subunits and two β subunits, with each subunit containing a heme molecule capable of binding oxygen. The structure and function of hemoglobin enable it to

[a] *Dongguan Key Laboratory of Screening and Research of Anti-inflammatory Ingredients in Chinese Medicine, School of Pharmacy, Guangdong Medical University, Dongguan 523808, China. E-mail: wsyt132@163.com*
[b] *Guangdong Key Laboratory of Nanomedicine, Shenzhen Institute of Advanced Technology, Chinese Academy of Sciences, Shenzhen 518055, China*
[c] *Department of Gastroenterology, the Tenth Affiliated Hospital of Southern Medical University (Dongguan People's Hospital), Dongguan 523000, China*
[d] *Institute of Nano Biomedicine and Engineering, School of Sensing Science and Engineering, School of Electronic Information and Electrical Engineering, Shanghai Jiao Tong University, 800 Dongchuan RD, Shanghai 200240, China*
[e] *Cancer Centre, Faculty of Health Sciences, University of Macau, Macau SAR, China*
†Electronic supplementary information (ESI) available. See DOI: https://doi.org/10.1039/d3nr05289c
‡These authors contributed equally to this work.

encapsulate and transport oxygen.[21] Using Hb to elevate the oxygen concentration within tumors, this combination therapy approach enhances the effectiveness of anti-tumor treatments.[22,23] However, few researchers have explored the simultaneous elevation of O_2 levels and increased ROS within cancer cells to improve therapeutic outcomes. Therefore, there is an urgent need to develop novel combination therapies to enhance the efficacy of catalytic treatments. Curcumin (Cur), a diketone compound extracted from the rhizomes of turmeric, exhibits diverse pharmacological activities such as anti-inflammatory and anti-tumor effects.[24] Cur, being a natural photosensitizer, can mediate the generation of singlet oxygen in photodynamic therapy (PDT) to kill tumor cells. Additionally, as a chemotherapeutic agent, it synergizes with PDT to exert anti-tumor effects.[25,26]

In this study, we constructed a composite magnetic nanosystem, utilizing a Hb-coloaded Fe_3O_4 based nanoenzyme and Cur (referred to as Fe_3O_4-Hb@cur), for enhancing ROS and designing catalytic reactions in cancer nanotherapy (Fig. 1). This strategy possesses the following characteristics: (1) Nanozymes exhibit inherent peroxidase-like activity, decomposing H_2O_2 into ·OH to induce tumor cell damage. (2) Oxygen

self-supply can be achieved through the encapsulation of Hb, and the increased O_2 can be activated by Cur to generate $^1O_2$ for tumor cell death, thereby enhancing the catalytic performance of the nanozymes. Based on this therapeutic approach, we report the preparation of a small-sized magnetic nanozyme with intrinsic oxygen supply (Fe_3O_4-Hb@cur), which demonstrates synergistic effects on tumor damage through combined photodynamic and catalytic therapy. In summary, our work highlights the tremendous potential of modulating the TME using intelligent nanosystems to enhance the effectiveness of various treatment modalities, potentially inhibiting tumor growth and achieving comprehensive effects on cancer. This has significant implications in the field of nanocatalytic medicine.

2. Experimental section

2.1. Materials

Curcuminoids (Cur) and hemoglobin (Hb) were purchased from Macklin Biochemical Co., Ltd (Shanghai, China). 3,3′,5,5′-Tetramethylbenzidine (TMB), 2′,7′-dichlorofluorescein diacetate (DCFH-DA), 4′,6-diamidino-2-phenylindole (DAPI) and 1,3-diphenylisobenzofuran (DPBF) were purchased from Aladdin Reagent Co., Ltd (Shanghai, China). Cy5.5 was purchased from Xi'an ruixi Biological Technology Co., Ltd. The cell counting kit was purchased from ZETA life. All reagents were of analytical grade and used without any purification.

2.2. Synthesis of Fe_3O_4

Monodisperse Fe_3O_4 nanoparticles with average diameters of around 15 nm were synthesized using a previously published protocol.[27] Afterwards, the product was precipitated with ethanol and redispersed in chloroform. The obtained Fe_3O_4 nanoparticles were then transferred into water by a polymer coating process, which was carried out by a published method.[28] Finally, Fe_3O_4 nanoparticles were stored in water at 4 °C for further use.

2.3. Synthesis of Fe_3O_4-Hb@cur

Under magnetic stirring, 2 mL of Fe_3O_4 (2 μM) was mixed with a 4 mL solution of Hb (dissolved in PBS at a concentration of 1 mg mL^{-1}) overnight. The mixture was then slowly added dropwise to 2 mL of cur (300 μM) and further blitzed overnight on a rotary mixer. The final product was concentrated using an ultrafiltration tube to 4 mL and stored at 4 °C.

2.4. Characterization of Fe_3O_4-Hb@cur

The morphological features of Fe_3O_4 and Fe_3O_4-Hb were analyzed using Transmission Electron Microscopy (TEM, JEOL JEM 2100F from Japan Electron). UV-vis absorption spectra of Fe_3O_4, cur, Hb, and Fe_3O_4-Hb@cur were recorded using an ultraviolet-visible spectrophotometer (Lambda25, PerkinElmer, USA). A Dynamic Light Scattering (DLS) analyzer (Malvern Instruments, UK) was used to measure the particle size of Fe_3O_4-Hb@cur. Electron Paramagnetic Resonance (EPR,
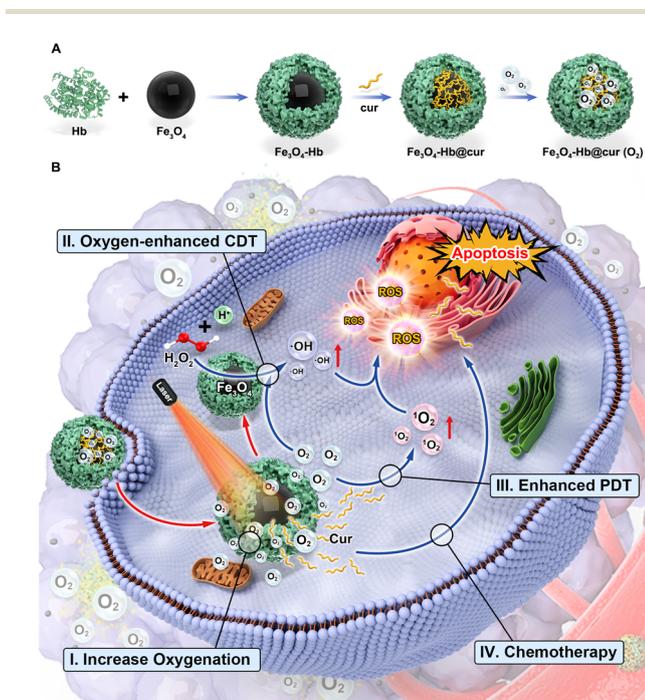
Fig. 1 A scheme of the preparation process (A) of the oxygen-supplying magnetic nanoparticle enzyme (Fe_3O_4-Hb@cur) and its mechanism for achieving photodynamic and catalytic therapy of tumor (B). In a hypoxic environment, oxygen molecules are released from Fe_3O_4-Hb@cur to overcome the oxygen-deficient TME. Hb carrying O_2 is co-loaded with the photosensitizer/chemotherapeutic agent cur, and upon NIR irradiation, it activates the surrounding molecular oxygen to generate a certain amount of $^1O_2$ for PDT. Simultaneously, O_2-enhanced Fe_3O_4 mediates CDT by producing ·OH through the Fenton reaction. Therefore, Fe_3O_4-Hb@cur achieves significant in vivo synergistic therapeutic effects to accomplish the mechanism of catalytic-photodynamic therapy for breast cancer.

BRUKER EMXPLU) was used to measure the signals of reactive oxygen species. The EDS (Energy Dispersive Spectrometer) used for detecting the elements, composition information, and concentration of the samples was Oxford Xplore 30. *In vitro* magnetic resonance (MR) images using T_2-weighted sequences were acquired using a 3.0 T clinical MR scanner (Erlangen, GER). The signal intensity in the region of interest (ROI) was measured for all T_2-weighted MR images. To calculate the relaxation rates (r_2, $1/T_2$), a range of concentrations of the Fe_3O_4-Hb@cur complex were measured. FL images were analyzed with the IVIS imaging system (CALIPER IVIS SPECTRUM). The collection parameters were Em = 700 nm and Ex = 640 nm. Fluorescence spectral scanning was performed using an FL970 fluorescence spectrophotometer (Tianmei, China).

2.5. Hemolysis assay

0.5 mL of blood sample was added to 1 mL of PBS solution and centrifuged at 4500 rpm for 5 min, and the red blood cells were separated from the serum. Then, the red blood cells were washed 5 times with PBS and resuspended in 5 mL of PBS. Next, 0.3 mL of the above-mentioned red blood cells was mixed with 1.2 mL of Fe_3O_4-Hb@cur at different concentrations (0–100 μM, prepared in PBS). The solution was gently mixed and allowed to stand at 25 °C for 4 h, followed by centrifugation to separate the red blood cells. The dissolved red blood cells could not be separated. The absorbance of the supernatant was then measured at a wavelength of 541 nm (mean ± SD, n = 3). Red blood cells treated with PBS and deionized water were used as negative and positive control groups, respectively. The percentage of hemolysis was calculated using the equation:

$$Hemolysis(\%) = ((OD\,sample - OD\,negative\,control)/$$
$$(OD\,positive\,control - OD\,negative\,control)) \times 100\%.$$

2.6. H_2O_2-dependent catalysis of Fe_3O_4-Hb@cur

Briefly, 10 μL TMB (1 mM) and 150 μL acetic acid buffer solution (pH 5.5) were added to acetic acid buffer solution (H_2O_2 + Fe_3O_4@cur, H_2O_2 + Fe_3O_4-Hb@cur, and 150 μL H_2O_2 (1 mM)), respectively. Degradation of TMB was monitored with UV-Visible absorbance at 652 nm 1 h after the reaction. The degradation of TMB was monitored by observing the change in UV-Visible absorbance to evaluate the peroxidase activity of Fe_3O_4. Specifically, different concentrations of Fe_3O_4-Hb@cur (3, 6, 9, 12, and 15 μM) were added to a mixture containing acetic acid buffer solution (pH 5.5) and H_2O_2 (1 mM), following the addition of 10 μL TMB (1 mM). The absorbance at 652 nm was immediately detected and the data were recorded continuously for 8 min.

2.7. Light-triggered ROS generation

Diphenylisobenzofuran (DPBF) was used in this experiment to trap the $^1O_2$ produced by Fe_3O_4@cur under light conditions. We prepared Fe_3O_4@cur (Fe_3O_4 (2 μM, 15 μL) + cur (300 μM, 150 μL) + 300 μL PBS) and Fe_3O_4-Hb@cur (Fe_3O_4 (2 μM, 15 μL)

+ cur (300 μM, 150 μL) + Hb (1 mg mL^{-1}, 50 μL) + 250 μL PBS). 100 μL of the above samples were taken and mixed with 10 μL DPBF (20 mM) at 25 °C. Fe_3O_4@cur and Fe_3O_4-Hb@cur (300 μM as cur) and DPBF (20 mM) were irradiated with a 660 nm laser (0.5 W cm^{-2}) for 1, 2, 3, 4, or 5 min, respectively. Subsequently, the absorbance was recorded at a wavelength of 405 nm using a microplate reader.

2.8. Cell culture

4T1 mouse mammary adenocarcinoma cells were procured from Beina Biotech Co., Ltd and maintained in culture medium (DMEM) supplemented with 10% (v/v) fetal bovine serum and a 1% penicillin–streptomycin mixture. The cells were cultured under standard conditions (5% CO_2, 37 °C).

2.9. Cell uptake of Fe_3O_4-Hb@cur

4T1 cells were inoculated in confocal culture dishes at a density of 1×10^5 cells per dish and cultured in 5% CO_2 at 37 °C or 24 h. In 300 μM Fe_3O_4-Hb@cur after replacing medium, the cells were subjected to further different incubation times (1 h, 5 h, 9 h). Subsequently, the culture medium was aspirated, and the cells were washed three times with PBS. Paraformaldehyde was then added for an 8-minute incubation period to fix the cells. After removing the fixative, DAPI was added and incubated for 20 min. The cell nuclei were stained with DAPI in the co-localization experiments. The cells were observed using a confocal laser scanning microscope (CLSM) with an excitation wavelength of 471 nm for cur and 405 nm for DAPI.

2.10. Cell viability

The viability of 4T1 cells treated with different concentrations of PBS (as control), Fe_3O_4, Fe_3O_4@cur, Fe_3O_4-Hb@cur, Fe_3O_4@cur + laser, and Fe_3O_4-Hb@cur + laser was determined. The 4T1 cells were cultured in 96-well plates at an initial density of 10^4 cells per well and with overnight incubation at 37 °C. After that, gradient concentrations of Fe_3O_4, Fe_3O_4@cur and Fe_3O_4-Hb@cur were introduced and co-incubated with the cells for 24 h. A 100 μL medium solution containing 10 μL of CCK-8 was added to each well and incubated with the cells for 0.5 h. The optical density (OD) at 450 nm was measured using a microplate reader. Cell viability was calculated using the following formula:

$$Cell\,viability(\%) = (OD(sample) - OD(blank\,group))/$$
$$(OD(control) - OD(blank\,group)) \times 100.$$

2.11. Intracellular $^•OH$ detection

The intracellular $^•OH$ was measured *via* CLSM, and DCF served as a $^•OH$ indicator. The 4T1 cells were plated in 6-well plates and incubated at 37 °C overnight. Then, the cells were treated with different formulations (PBS (as a control), Fe_3O_4@cur, Fe_3O_4-Hb@cur, Fe_3O_4@cur + laser (Fe_3O_4@cur (+)) and Fe_3O_4-Hb@cur + laser (Fe_3O_4-Hb@cur (+)) (300 μM as cur)) for 12 h. Next, after washing the cells with PBS several times, the DCF solution (10 μM) was added and incubated

with the cells for 30 min. Finally, the cells were observed by CLSM.

2.12. Animal model

Female BALB/c mice aged 6 weeks and weighing 18–22 g were procured from Zhuhai Baishitong Biotechnology Co., Ltd. Subsequently, 4T1 cells which were suspended in 100 μL of phosphate-buffered saline (PBS) at a concentration of 3×10^6 were inoculated into the subcutaneous site of the right hind limb of each BALB/c mouse. The tumor volume was estimated every other day according to the following formula: (length × width^2)/2. All animal procedures were performed in accordance with the Guidelines for Care and Use of Laboratory Animals of Guangdong Medical University and approved by the Animal Ethics Committee of Guangdong Medical University (GDY2204043).

2.13. Monitoring the distribution of drugs in tumor-bearing mice

The distribution of nanoparticles was studied using the 4T1 mouse breast cancer model. Upon reaching a tumor volume of 150 mm^3, mice bearing tumors were randomly assigned into groups (n = 3) and received intravenous injections of either free Cy5.5 (2 mg kg^{-1}) or Cy5.5@ Fe$_3$O$_4$-Hb@cur (2 mg kg^{-1} of free Cy5.5). At specified time points after injection (1, 2, 4, 8, 12, 24, and 48 h), fluorescence biodistribution was analyzed using the IVIS *in vivo* imaging system. The collection parameters were Em = 700 nm and Ex = 640 nm.

2.14. MRI evaluation

In order to evaluate the tumor accumulation of nanoparticles, 4T1 tumor-bearing mice were subjected to MRI imaging at different time intervals following intravenous administration of either PBS or Fe$_3$O$_4$-Hb@cur. The mice were intravenous injection with 100 μL of PBS or Fe$_3$O$_4$-Hb@cur (containing 2 μM Fe$_3$O$_4$). MRI intensity imaging and semi-quantitative analysis were conducted using a 3.0 T clinical MR scanner (Erlangen, GER) at two time points: immediately after injection and 3 hours post-injection.

2.15. *In vivo* synergistic photodynamic and catalytic antitumor therapy

A 4T1 xenograft tumor model was established as mentioned above for evaluation of antitumor efficacy. The mice were then randomly separated into five groups (n = 6 mice per group): saline (as a control group), Fe$_3$O$_4$, Fe$_3$O$_4$@cur, Fe$_3$O$_4$-Hb@cur, Fe$_3$O$_4$@cur + laser (Fe$_3$O$_4$@cur (+)) and Fe$_3$O$_4$-Hb@cur + laser (Fe$_3$O$_4$-Hb@cur (+)). Therapeutic measures were commenced when the tumors reached a volume of approximately 150 cubic millimeters. On day 0, mice received combined therapy *via* tail vein injection. The tumor size and body weight were documented for each mouse from day 0 to day 16, and the tumor volume V was computed as $V = W^2 \times L/2$ (W and L are the shortest and longest diameters of the tumor, respectively). After 16 days of treatment, all mice were euthanized, and the major organs and tumor tissues were collected for further analysis.

2.16. Statistical analysis

All statistical analyses were analyzed using GraphPad Prism version 9 software. Experimental data were collected three times or more. The results were expressed as means ± standard deviation. Statistical analysis of the differences between two groups was conducted using a two-tailed Student's *t*-test. Difference between the two groups was considered statistically significant when the two-sided *P*-value was less than 0.05, where all significant values were indicated as follows: *P < 0.05, **P < 0.01, and ***P < 0.001.

3. Results and discussion

3.1. Construction and characterization of the Fe$_3$O$_4$-Hb@cur nanoplatform

In our study, homogeneous Fe$_3$O$_4$ nanoparticles with the average size of 15 nm were prepared by the thermal decomposition method, and after phase transfer into aqueous solution by polymer coating, a large number of carboxyl groups on their surface can then physically adsorb proteins (such as Hb) through electrostatic interactions. Small-sized magnetic nanozymes (Fe$_3$O$_4$-Hb) were further created by loading the Hb shells on the surface of Fe$_3$O$_4$ nanoparticles. The cavities of Hb can easily be loaded with many small molecule drugs (such as cur). Then, a photosensitizer/chemotherapeutic drug, cur, is loaded into the Fe$_3$O$_4$-Hb structure to obtain Fe$_3$O$_4$-Hb@cur. Therefore, the interaction during the formation of Fe$_3$O$_4$-Hb@cur is through physical absorption. Finally, oxygen is introduced into the solution to obtain Fe$_3$O$_4$-Hb@cur (O$_2$). Representative transmission electron microscopy (TEM) images show that the prepared nanozyme in this design have a single spherical morphology with an average diameter of about 15 nm (Fig. 2A). Notably, the successful encapsulation of Hb can be evidenced by the appearance of white halos on the surface of Fe$_3$O$_4$-Hb after Hb encapsulation of Fe$_3$O$_4$ (Fig. 2B). The dispersion of Fe$_3$O$_4$-Hb@cur was evaluated by dynamic light scattering (DLS). The DLS measurements indicate that Fe$_3$O$_4$-Hb@cur is homogeneous and well dispersed, with an average particle size of approximately 30 nm (Fig. S1†). Small-sized nanoparticles facilitate drug uptake and penetration within the tumor owing to elevated permeability and retention (EPR) effects.[29,30] As shown in the UV-vis spectra, due to the interaction between the carrier during cur loading, a red shift occurs in the peak position. As shown in Fig. 2C, the UV absorption peak of Fe$_3$O$_4$-Hb@cur matches the peak shape of cur. This absorption red shift demonstrates the successful encapsulation of cur in Fe$_3$O$_4$-Hb@cur. Moreover, the spectra changed significantly after Hb encapsulation with a strong absorption at 410 nm, indicating the formation of the Hb layer. The Fe$_3$O$_4$-Hb@cur sample shows both Hb and Fe$_3$O$_4$ absorption peaks after cur and Hb-bound Fe$_3$O$_4$. The successful loading of Cur was indicated by the change in the zeta potential, which was −15 mV for Fe$_3$O$_4$, −0.15 mV for cur, and −5.5 mV for the synthesized Fe$_3$O$_4$-Hb (Fig. S2†). Subsequently, we tested the zeta potential of the final product,
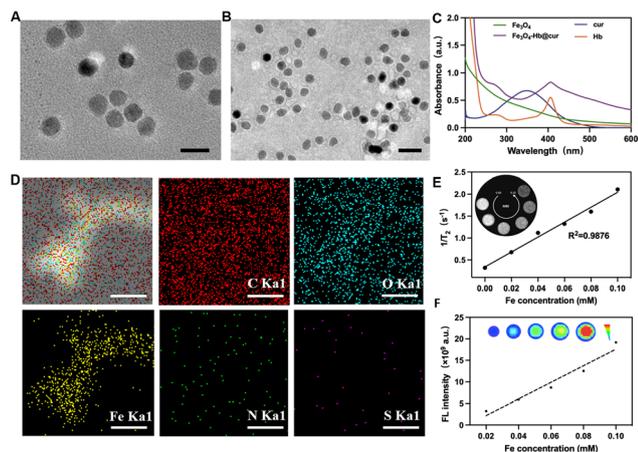
Fig. 2 Structural and compositional characterization of the Fe_3O_4-Hb@cur magnetic nanozyme. TEM images of (A) Fe_3O_4, scale bar: 25 nm, and (B) Fe_3O_4-Hb, scale bar: 50 nm. (C) UV-vis spectra of Fe_3O_4, cur, Hb, and Fe_3O_4-Hb@cur NPs. (D) Dark-field TEM image and the corresponding elemental mapping of C, O, Fe, N, and S of Fe_3O_4-Hb@cur. Scale bar: 30 nm. (E) Longitudinal relaxation rates ($1/T_2$) of Fe_3O_4-Hb@cur solution treated with pH 7.4 as a function of Fe concentration. The following images show T_2-weighted MR images of Fe_3O_4-Hb@cur after treatment at a pH of 7.4. (F) FL intensity of Fe_3O_4-Hb@cur solution at 673 nm as a function of Fe concentration. The inset shows the corresponding FL images of Fe_3O_4-Hb@cur solution.

Fe_3O_4-Hb@cur, and the result was −1.5 mV. The loading of cur successfully neutralized the electronegativity of the final product. Moreover, we compared the fluorescence spectra of cur, Fe_3O_4-Hb@cur, and Fe_3O_4-Hb in the range of 450–700 nm under the excitation wavelength of cur (420 nm) (Fig. S3†). The results revealed that cur and Fe_3O_4-Hb@cur exhibited identical fluorescence peak positions, providing evidence for the successful loading of cur onto Fe_3O_4-Hb@cur. However, Fe_3O_4-Hb did not exhibit the same fluorescence peak. In addition, elemental mapping was performed to reveal the distribution of the elements C, N, O, S, and Fe in Fe_3O_4-Hb@cur (Fig. 2D). Fe_3O_4-Hb@cur nanoenzymes contain elements C, O, Fe, N and S. The successful synthesis of Fe_3O_4-Hb@cur was further demonstrated by the combination of UV-vis and zeta potential. The atomic percentages of the elements in the obtained Fe_3O_4-Hb@cur solution were as follows: C 86.41%, N 0.08%, O 13.24%, S 0.01%, and Fe 0.25%. The zeta potential, changes in DLS size, TEM imaging, and absorption peaks indicate the successful preparation of Fe_3O_4-Hb@cur. Finally, we performed hemolysis experiments to demonstrate that Fe_3O_4-Hb@cur has good biocompatibility and safety (Fig. S4†).

Magnetic resonance imaging (MRI) and fluorescence intensity (FL) experiments were performed in order to reveal the bioimaging capabilities of Fe_3O_4-Hb@cur. As shown in Fig. 2E, MRI images of Fe_3O_4-Hb@cur at different concentrations were acquired using a clinical magnetic resonance scanner at room temperature. The transverse relaxivity (r_2) measurement for iron concentration was found to be 17.04 mM^{-1} s^{-1}, indicating a linear relationship. Fe_3O_4-Hb@cur exhibited a decrease in

signal intensity (shortening of T_2 relaxation time) in T_2-weighted imaging with increasing concentration.[31,32] The fluorescence properties of the nanoparticles were subsequently investigated by attaching Cy5.5 to Fe_3O_4-Hb@cur. We compared the fluorescence spectra of Cy5.5, Fe_3O_4-Hb@cur-Cy5.5, and Fe_3O_4-Hb@cur in the range of 500–1000 nm at an excitation wavelength of Cy5.5 (673 nm). The results revealed that Cy5.5 and Fe_3O_4-Hb@cur-Cy5.5 exhibited identical fluorescence peak positions, providing evidence for the successful loading of Cy5.5 onto Fe_3O_4-Hb@cur (Fig. S5†). Cy5.5 has a specific fluorescence emission upon excitation at 673 nm, which can be further used for *in vivo* imaging. The FL signal intensity in aqueous solution under 673 nm laser excitation was linearly correlated with the concentration of Fe (Fig. 2F). Overall, Fe_3O_4-Hb@cur combined with Cy5.5 showed excellent MRI and FL imaging properties, which could be used as an ideal MRI contrast and fluorescence indicator for therapeutic diagnostic applications.

3.2. H_2O_2-dependent catalysis of Fe_3O_4-Hb@cur

In the presence of acetic acid buffer solution (pH 5.5), Fe_3O_4 can exhibit peroxidase-like activity that catalyzes the degradation of H_2O_2 to generate highly toxic ˙OH for chemodynamic cancer therapy.[33–35] 3,3′,5,5′-Tetramethylbenzidine (TMB), oxidized by ˙OH, changes the color of the mixture from colorless to blue-green with a typical absorbance peak at 652 nm. Therefore, it can be used to detect the generated ˙OH. As shown in Fig. 3A, H_2O_2 in the absence of Fe_3O_4 based nanozymes cannot induce the Fenton reaction without obvious absorption at 652 nm. When H_2O_2 is mixed with Fe_3O_4-Hb@cur or Fe_3O_4@cur, an evident absorption at 652 nm from TMB was detected and the color changes of the solution was recorded, indicating the peroxidase-like activity of Fe_3O_4. The
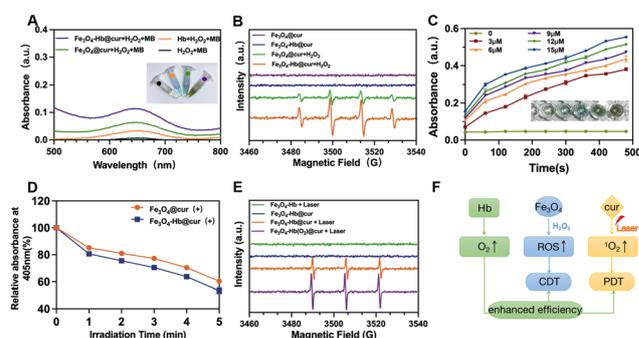
Fig. 3 Characterization of the enzyme-like activity of the Fe_3O_4-Hb@cur nanozyme. (A) UV-vis absorption spectra of TMB in different groups with pH 5.5. The inset shows the corresponding visual color changes. Generation of $^1O_2$ signals (B) and ˙OH signals (E) recorded by ESR spectra at different conditioned stimuli, respectively. (C) H_2O_2-concentration dependence of UV-vis absorbance changes employing a TMB probe at 652 nm. (D) Changes in DPBF absorbance at 405 nm were observed after treating it with Fe_3O_4@cur and Fe_3O_4-Hb@cur NPs under a 660 nm laser for different irradiation times. (F) Schematic representation of possible mechanisms of oxygen enhancement and tumor-expressed ROS under Fe_3O_4-Hb@cur conditions.

generated ˙OH can be used for chemokinetic therapy and combined with chemotherapy to achieve multi-mode cancer therapy. When Hb was loaded, the peak absorbance increased, indicating that O_2 carried on Hb enhanced the peroxidase activity of Fe_3O_4 and promoted the generation of ˙OH. According to reports, the catalytic activity is associated with the generation capacity of ˙OH.[36] Therefore, the detection of ˙OH production using electron spin resonance (ESR) is consistent. Compared to Fe_3O_4@cur and Fe_3O_4-Hb@cur groups, the ˙OH signal was detected in both Fe_3O_4@cur and Fe_3O_4-Hb@cur groups containing H_2O_2. Furthermore, a more pronounced signal was detected in the Fe_3O_4-Hb@cur group containing H_2O_2 (Fig. 3B).

To systematically evaluate the catalytic performance of Fe_3O_4-Hb@cur, We investigated the ability of the nanoenzyme to generate ˙OH under different pH conditions and found that our studied material only produced a significant amount of ˙OH at pH 5.5. In contrast, very little ˙OH was generated at pH 6.5 or pH 7.4. This indicates that a certain amount of H^+ is required for Fe_3O_4-Hb@cur to exhibit positive feedback, which is beneficial for the effective functioning of the nanoenzyme after entering tumor cells (Fig. S6†). Moreover, different concentrations (3, 6, 9, 12, and 15 μM) of H_2O_2 were added to Fe_3O_4-Hb@cur in the presence of TMB (1 mM). The absorbance was then monitored as a function of time and H_2O_2 concentration to observe the dependence (Fig. 3C). Therefore, Fe_3O_4-Hb@cur based enzyme can be used as an efficient-mimicking enzyme for cancer therapy.

3.3. O_2-enhanced PDT effect *in vitro*

Oxygen is an essential element in the photodynamic therapy process, yet the hypoxic TME greatly reduces the efficacy of PDT for solid tumors. Therefore, an adequate supply of oxygen at the tumor site is very important for generating $^1O_2$ to treat tumors.[37,38] In this study, the absorption of DPBF at 405 nm was irreversibly quenched by $^1O_2$, and thus was used as a probe for monitoring the production of $^1O_2$ by Fe_3O_4 @cur and Fe_3O_4-Hb@cur under 660 nm light irradiation.[39,40] At various time points, the absorption values of the samples at 405 nm were continuously recorded using an UV-Vis spectrophotometer. As shown in Fig. 3D, at the fifth minute, there was a significant decrease in absorbance values for both groups. However, the group containing encapsulated O_2 in Fe_3O_4-Hb@cur exhibited a stronger signal. In particular, the Fe_3O_4-Hb@cur group showed a lower absorbance value, around 50%, indicating an increased generation of $^1O_2$. This observation suggests that the presence of Fe_3O_4-Hb@cur (O_2) enhances the production of $^1O_2$. In summary, these results indicate that the release of O_2 is crucial for the antitumor effect of PDT. The loading of O_2 by Hb enhances the PDT efficacy of Fe_3O_4@cur, which has the potential to become a more efficient photocatalyst.

To further demonstrate the applicability of Fe_3O_4-Hb@cur in PDT, the ESR technique was employed to investigate the generation of $^1O_2$ under near-infrared laser irradiation. As shown in Fig. 3E, in the absence of light and the photosensiti-

zer cur, no signal of $^1O_2$ was detected. Compared to the other groups, the Fe_3O_4-Hb@cur group carrying O_2 exhibited a stronger signal of $^1O_2$, indicating that O_2 effectively enhanced the PDT effect. This finding highlights the crucial role of O_2 in improving PDT within a hypoxic TME. These results emphasize the potential of Fe_3O_4-Hb@cur(O_2) in enhancing the efficacy of PDT, particularly under hypoxic conditions, and provide promising prospects for cancer treatment. The aforementioned principle and mechanism are presented using a schematic diagram labeled in Fig. 3F.

3.4. Cellular uptake of Fe_3O_4-Hb@cur

The cellular uptake behavior of Fe_3O_4-Hb@cur was studied by Confocal Laser Scanning Microscopy (CLSM). As shown in Fig. 4A, intense fluorescence of cur was observed in the cytoplasm, indicating the successful uptake of Fe_3O_4-Hb@cur by 4T1 cells. With the prolongation of the incubation time, cur was significantly accumulated in the nucleus, which indicated that after the cellular uptake of Fe_3O_4-Hb@cur magnetic nanoenzymes, the Fe_3O_4 nanocarriers were ruptured in acidic lysogeny and the intracellular cur was gradually released. Semiquantitative analysis of CLSM images in Fig. 4B showed that the uptake of Fe_3O_4-Hb@cur by 4T1 tumor cells increased with prolonged incubation times (1, 5, and 9 h).

3.5. Laser enhances cytotoxicity and cell apoptosis

Next, we investigated the synergistic photodynamic and catalytic effects of Fe_3O_4-Hb@cur as a nanoenzyme on tumor photodynamic and catalysis *in vitro*. We firstly tested the cytotoxicity of Fe_3O_4-Hb@cur in the dark. The release of cur and the generation of ˙OH could significantly enhance the synergistic photodynamic/catalytic treatment of cancer with the help of enhanced O_2 concentration. The synergistic anticancer effect of the drugs was studied using cell viability assay kit (CCK-8) analysis. When electronically coupled reagents are
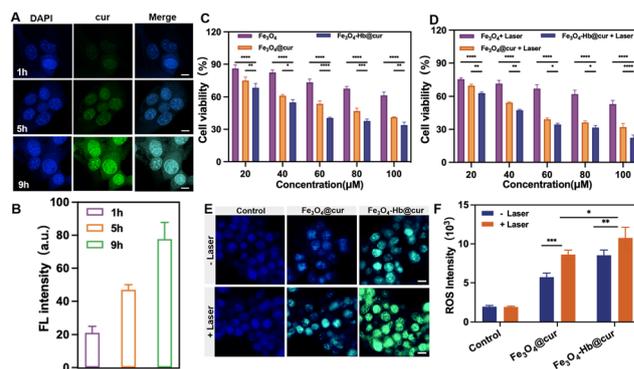
Fig. 4 Cellular uptake (A) and relative fluorescence intensity (B) of Fe_3O_4-Hb@cur after 1, 5, and 9 h of co-incubation with 4T1 cells. Scale bar: 8 nm. Cytotoxicity at different concentrations of Fe_3O_4, Fe_3O_4@cur, and Fe_3O_4-Hb@cur against 4T1 cells in the dark (C) and after 30 seconds of laser irradiation (D). Data are presented as means ± SD (*n* = 3 per group). ***P < 0.001 and ****P < 0.0001. Detection of ROS levels (E) with the relative fluorescence intensity (F) after different treatments in DCFH-DA-stained 4T1 cells for 12 h. Scale bar: 10 nm.

present, WST-8 (2-(2-methoxy-4-nitrophenyl)-3-(4-nitrophenyl)-5-(2,4-dithiobenzyl)-2H-tetrazole monosodium salt) undergoes reduction by mitochondrial dehydrogenase, resulting in the formation of a water-soluble, orange-yellow product (formazan) that produces methane. The optical density (OD) of the formazan product can be measured at 450 nm using an enzyme marker. It can indirectly reflect the number of living cells. As shown in Fig. 4C, Fe_3O_4-Hb@cur showed stronger cell damage than Fe_3O_4@cur or free Fe_3O_4 at each concentration, which was attributed to the much stronger effect of synergistic photodynamic therapy/catalytic treatment than PDT or catalytic treatment alone. Furthermore, the synergistic killing effect of O_2 for both treatments was confirmed.

To evaluate the photodynamic conversion efficiency of cur, the cells were treated with a 660 nm laser (0.5 W cm^{-2}, 2 min). The relative survival was determined after 24 h using a colorimetric assay with tetramethyl azole salts. As shown in Fig. 4D, both types of irradiation with 660 nm excitation light exhibited enhanced drug cytotoxicity. Compared with the unenhanced light irradiation (Fe_3O_4-Hb@cur), the combined Fe_3O_4-Hb@cur under laser treatment showed the best killing effect on cancer cells at different concentrations (Fig. S7†). Therefore, the high antitumor effect of Fe_3O_4-Hb@cur in these treatments was mainly attributed to the enhanced catalytic therapy induced by the self-contained O_2 of the magnetic nanoenzymes as well as PDT.

### 3.6. Light-triggered ROS generation

Fe_3O_4@cur can react with local H_2O_2 to produce highly toxic ˙OH in the acidic tumor microenvironment. In this study, 2′,7′-dichlorofluorescein diacetate (DCFH-DA) was used to detect the intracellular ROS levels to confirm whether light irradiation increased intracellular ROS levels. Intracellular ROS can catalyze the generation of fluorescent 2,7-dichlorofluorescent diacetate (DCF) from non-fluorescent DCFH, allowing it to be used as a ROS probe to dynamically monitor ROS by fluorescent signals.[41,42] As shown in Fig. 4E, little fluorescence was observed in 4T1 cells without any treatment, regardless of whether light was increased, indicating basal intracellular ROS levels. In contrast, ROS levels were significantly up-regulated after 4T1 cells co-cultured with Fe_3O_4@cur or Fe_3O_4-Hb@cur, which was shown as the intense green fluorescence in CLSM images (Fig. S8†). Thus, Fe_3O_4@cur contributed to the improvement of ROS production. Furthermore, a higher fluorescence intensity was detected in Fe_3O_4-Hb@cur treated cells, proving that O_2 in Fe_3O_4-Hb@cur was successfully involved in $^1O_2$ generation. This further confirms that the PDT toxicity of Fe_3O_4@cur can be enhanced by the increase of O_2.

3.7. Biodistribution and tumor-targeting activity of Fe_3O_4-Hb@cur

The biological distribution and anticancer effect of Fe_3O_4-Hb@cur *in vivo* was further investigated in 4T1 Tumor-bearing Balb/c Mice. With its long excitation and emission wavelengths, Cy5.5 exhibits the capability of penetrating deep tissues, making it an ideal probe for the detection of tumor

accumulation. To visually observe the biological distribution of Fe_3O_4-Hb@cur *in vivo*, intravenous Fe_3O_4-Hb@cur was labeled with Cy5.5 (denoted as Fe_3O_4-Hb@cur-Cy5.5). Imaging and quantification of the whole body and major organs were recorded and presented using an IVIS spectrum small animal imaging system at different time intervals after intravenous injection (Fig. 5A and B). Due to the enhanced permeability and retention (EPR) effect of tumor, the material accumulates at the tumor site.[43–45] As time progressed, the fluorescence intensity of the Fe_3O_4-Hb@cur-Cy5.5 group remained consistently stronger than that of the Cy5.5 group. Free Cy5.5 exhibited a shorter circulation half-life in mice, while the Fe_3O_4-Hb@cur-Cy5.5 group demonstrated a prolonged circulation time. At 12 and 48 h post-injection, the *in vivo* fluorescence intensity of the Fe_3O_4-Hb@cur-Cy5.5 group was 1.76-fold and 3.05-fold higher, respectively, compared to free Cy5.5. This indicates effective accumulation of Fe_3O_4-Hb@cur-Cy5.5 within the tumor (Fig. 5C). Moreover, *in vitro* imaging and quantitative analysis of major organs in Fig. 5D showed that there was still a strong fluorescence signal in Fe_3O_4-Hb@cur-
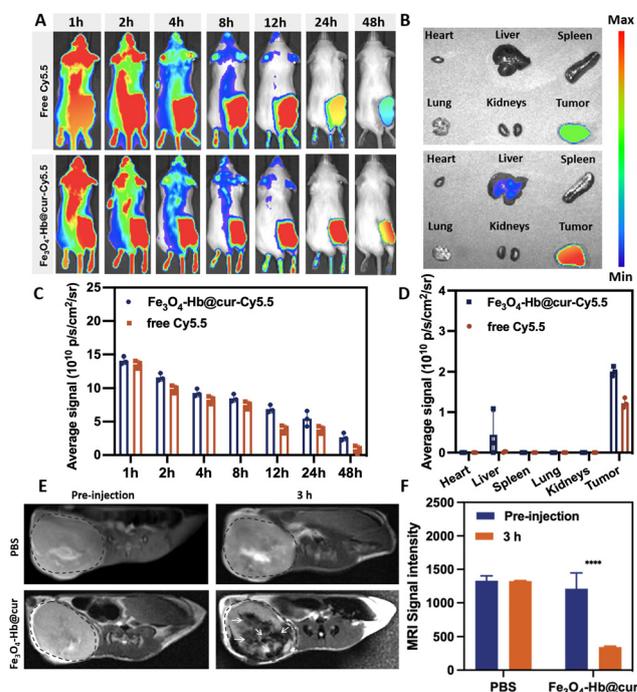
Fig. 5 *In vivo* imaging study of Fe_3O_4-Hb@cur. (A and B) *In vivo* fluorescence images of 4T1 tumor-bearing mice dissected organs, and tumors after intravenous injected with free Cy5.5 or Fe_3O_4-Hb@cur-Cy5.5 for different times. (C) Quantitative mean fluorescence intensity analysis of tumor tissues at different time intervals (*n* = 5 per group). ***P < 0.001 and ****P < 0.0001. (D) Fluorescence intensities of the organs and tumors collected at different times. (E) Over a period of time following the intravenous administration of Fe_3O_4-Hb@cur nanoparticles, *in vivo* magnetic resonance (MR) imaging was performed in the tumor region to monitor changes. (F) T_2-Weighted magnetic resonance imaging of mouse tumors at 0 h and 3 h after tail vein injection of Fe_3O_4-Hb@cur nanoparticles.

Cy5.5 in the tumor and liver 48 h after injection, further confirming the long cycle and EPR effect of Fe_3O_4-Hb@cur.

Furthermore, MRI was employed to evaluate the accumulation of Fe_3O_4-Hb@cur. To evaluate the accumulation of Fe_3O_4-Hb@cur *in vivo*, T_2-weighted MRI was performed by utilizing 4T1 breast cancer xenografts after intravenous administration of Fe_3O_4-Hb@cur. Fig. 5E shows the observed MRI signal, which increased over time. Furthermore, further analysis was conducted on the statistically semi-quantitative T_2 signal intensity. The signal intensity of Fe_3O_4-Hb@cur was the lowest at 3 h, while the signal intensity of the PBS group showed no difference at 3 h, consistent with the imaging results (Fig. 5F). This further confirms the strong tumor accumulation ability of Fe_3O_4-Hb@cur through prolonged circulation and the EPR effect. Therefore, Fe_3O_4-Hb@cur nanoparticles can effectively target tumor sites.
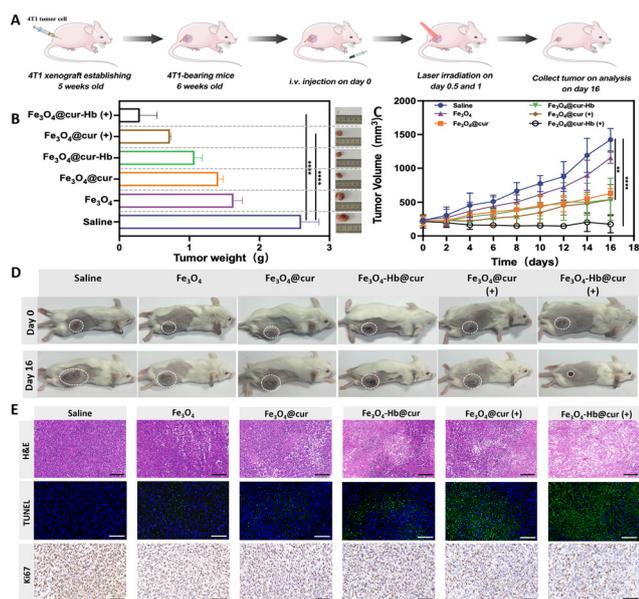
3.8. *In vivo* synergistic photodynamic and catalytic antitumor effects of Fe_3O_4-Hb@cur

The combined therapeutic effect of Fe_3O_4-Hb@cur, which exhibits effective tumor targeting and PDT effects, was evaluated by inoculating 4T1 cells in BALB/c mice. As shown in Fig. 6A, the mice were randomly divided into 5 groups (6 mice per group), and each group was injected with 100 μL saline (as a control), Fe_3O_4, Fe_3O_4@cur, Fe_3O_4-Hb@cur, Fe_3O_4@cur + laser (Fe_3O_4@cur (+)) and Fe_3O_4-Hb@cur + laser (Fe_3O_4-

Fig. 6 (A) Schematic illustration showing the time line of the efficacy study. (B) Tumor weights in each group at the end of 16 days of treatment. (C) Tumor volume curves of 4T1 tumor-bearing mice with different treatments at 16 days. Obvious inhibition occurred in the Fe_3O_4-Hb@cur (+) group (***P < 0.001 and ****P < 0.0001). (D) Representative images of the 4T1-bearing mice at day 0 and day 16 after different treatments. (E) Tumor histological images of H&E staining and Ki67 staining of tumors after different treatments. Scale bar: 100 μm. TUNEL staining for apoptosis in tumors extracted from mice with different treatments (green, TUNEL; blue, and DAPI). Scale bar: 50 μm.

Hb@cur (+)) through the caudal vein (an equivalent dose of 25 mg kg^{-1} cur or 0.75 mg kg^{-1} Fe_3O_4). When the tumor volume reached approximately 150 mm^3, the treatments were initiated. Irradiation was scheduled at 12 and 24 h after drug injection based on the results of biodistribution of nanoparticles. Subsequently, the tumors were exposed to a 660 nm laser with a power density of 0.5 W cm^{-2} for a duration of 5 minutes. Fig. 6B–D illustrates that only the Fe_3O_4-Hb@cur(+) group exhibited a significant inhibition of tumor volume and tumor load, following the completion of the treatments, whereas the other four groups displayed only slight tumor growth suppression. In contrast, the Fe_3O_4-Hb@cur treatment group observed a strong inhibitory effect on the tumor, which was completely suppressed within 16 days of tumor growth. The therapeutic effect was clearly observed in post-treatment mouse tumor photographs (Fig. 6B). It is worth noting that the Fe_3O_4-Hb@cur nanoparticle group also demonstrated a moderate level of antitumor activity, further confirming the important role of O_2 carried by Hb in enhanced catalytic therapy and PDT. Additionally, Fe_3O_4@cur also exhibited certain therapeutic efficacy, which may be attributed to the ability of Fe_3O_4@cur to effectively accumulate tumors and administer chemotherapy. Overall, there were few significant fluctuations in the body weights of the mice after the various treatments, suggesting that Fe_3O_4 nanoparticles can have negligible side effects in the tumor treatment at the doses used (an equivalent dose of 25 mg kg^{-1} cur or 0.75 mg kg^{-1} Fe_3O_4) (Fig. S9†).
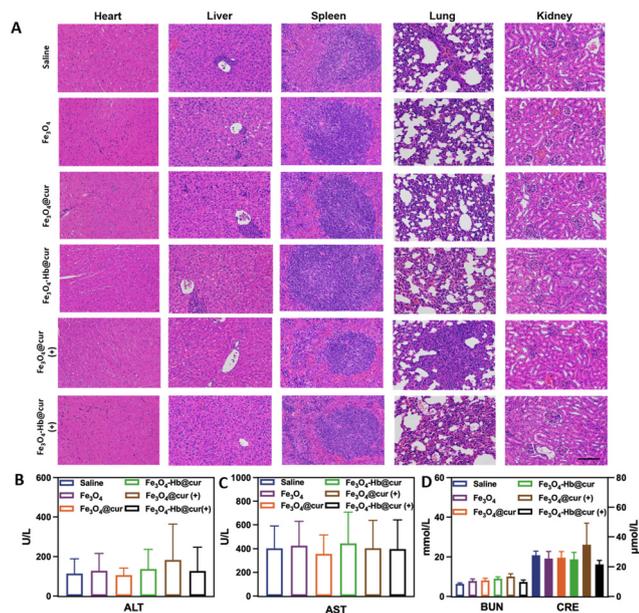
At the end of the treatment, the mice were euthanized, and tumor tissues were dissected and stained for histological analysis (Fig. 6E). Hematoxylin and eosin (H&E) staining of the tumor tissues revealed typical characteristics: enlarged and darkly stained cell nuclei with minimal cytoplasm. Compared to the saline group, the treatment group with Fe_3O_4-Hb@cur (+) showed severe cell necrosis in the tumor tissue, while other groups exhibited varying degrees of tumor necrosis induction. Additionally, the TUNEL assay and Ki67 immunohistochemistry were performed to further support the above findings, indicating that Fe_3O_4-Hb@cur had the strongest positive reaction and the most significant therapeutic effect. Therefore, Fe_3O_4-Hb@cur demonstrated effective tumor targeting and synergistic anti-tumor activity.

3.9. Biosafety evaluation

To investigate the *in vivo* toxicity of the nanomedicine, on the 16th day of treatment, the mice were killed by cervical dislocation, and tumors were isolated and weighed. Comprehensive analysis of blood, physiological, and biochemical parameters of the mice was conducted. H&E staining was performed on major organ tissue samples (Fig. 7A). No significant organ damage or inflammatory injury was observed in any of the treatment groups compared with the physiological saline group, indicating that photodynamic and catalytic synergistic therapies had no significant impact on the organ function of mice. To assess liver and kidney damage, blood levels of AST, ALT, BUN and CRE were measured and analyzed. No significant differences occurred and remained within the

Fig. 7 *In vivo* biosafety of Fe₃O₄-Hb@cur. (A) H&E-stained images of major organs (heart, liver, spleen, lungs, and kidneys) harvested from 4T1 tumor-bearing mice. Scale bar, 100 nm. Each mouse was treated with a single dose of saline (as a control), Fe$_3$O$_4$, Fe$_3$O$_4$@cur, Fe$_3$O$_4$-Hb@cur, Fe$_3$O$_4$@cur + laser (Fe$_3$O$_4$@cur (+)) and Fe$_3$O$_4$-Hb@cur + laser (Fe$_3$O$_4$-Hb@cur (+)) through the caudal vein ((an equivalent dose of 25 mg kg^{-1} cur or 0.75 mg kg^{-1} Fe$_3$O$_4$)) through i.v. administration. Mice were sacrificed 16 days after drug administration. (B–D) The serology panel for biomarkers of body function and hepatic function of mice in the control and various Fe containing groups (an equivalent dose of 25 mg kg^{-1} cur or 0.75 mg kg^{-1} Fe$_3$O$_4$) after treatment for 16 days. n = 6 mice per group. AST: aspartate aminotransferase; ALT: alanine transaminase; BUN: blood urea nitrogen; and CRE: creatinine.

normal physiological range with regard to all these biomarkers (Fig. 7B–D). Therefore, all the measured parameters and pathological assessments indicated that Fe$_3$O$_4$, Fe$_3$O$_4$@cur, Fe$_3$O$_4$-Hb@cur, Fe$_3$O$_4$ @cur + laser and Fe$_3$O$_4$-Hb@cur + laser (at an equivalent dose of 25 mg kg^{-1} cur or 0.75 mg kg^{-1} Fe$_3$O$_4$) did not exhibit significant toxicity.

4. Conclusions

In summary, we reported a unique type of O$_2$ enhanced multifunctional nano-sonosensitizer platform using Fe$_3$O$_4$ and cur, encapsulated by Hb (Fe$_3$O$_4$-Hb@cur) successfully. Fe$_3$O$_4$ can catalyze the conversion of H$_2$O$_2$ to ˙OH through the Fenton reaction, while Hb can self-supply O$_2$, overcoming the hypoxia barrier of tumor cells. Working as a photosensitizer, cur was effectively stimulated by low-intensity laser irradiation at 660 nm and this excited the surrounding O$_2$ to generate a certain amount of ^{1}O$_2$ for tumor inhibition. Therefore, Fe$_3$O$_4$-Hb@cur exhibited a synergistic CDT/PDT anticancer ability *in vitro* and *in vivo*. Additionally, Fe$_3$O$_4$-Hb@cur remarkably enhanced T_2-weighted MR imaging. Overall, Fe$_3$O$_4$-Hb@cur

with MR imaging-guided synergistic cancer therapy has the potential for bio-application in the bio-nanomedicine field.

Author contributions

X.Y.C. directed and conceived this project with input from T.Y. and Q.Z. synthesized the materials, performed most of the experimental work, and wrote the draft of the manuscript. T.T. X., R.D. and D.Z. performed the experimental data analysis. G. Q.C. and W.C.Z. performed the theoretical study. H.P. and J.J. H. designed the project. All the authors discussed the results and contributed to the writing and revision of the manuscript.

Conflicts of interest

There are no conflicts to declare.

References

1 S. Yao, M. Zheng, S. Wang, T. Huang, Z. Wang, Y. Zhao, W. Yuan, Z. Li, Z. L. Wang and L. Li, *Adv. Funct. Mater.*, 2022, **32**, 2209142.

2 S. Yao, X. Zhao, X. Wang, T. Huang, Y. Ding, J. Zhang, Z. Zhang, Z. L. Wang and L. Li, *Adv. Mater.*, 2022, **34**, 2109568.

3 Y. Nie, W. Chen, Y. Kang, X. Yuan, Y. Li, J. Zhou, W. Tao and X. Ji, *Biomaterials*, 2023, **295**, 122031.

4 L. Hou, F. Gong, Z. Han, Y. Wang, Y. Yang, S. Cheng, N. Yang, Z. Liu and L. Cheng, *Angew. Chem., Int. Ed.*, 2022, **61**, e202208849.

5 X. Wang, Q. Chen, Y. Zhu, K. Wang, Y. Chang, X. Wu, W. Bao, T. Cao, H. Chen, Y. Zhang and H. Qin, *Signal Transduction Targeted Ther.*, 2023, **8**, 277.

6 L. Chen, Z. Mao, Y. Wang, Y. Kang, Y. Wang, L. Mei and X. Ji, *Sci. Adv.*, 2022, **8**, eabo7372.

7 C. Zhang, J. Huang, Z. Zeng, S. He, P. Cheng, J. Li and K. Pu, *Nat. Commun.*, 2022, **13**, 3468.

8 C. Cao, N. Yang, X. Wang, J. Shao, X. Song, C. Liang, W. Wang and X. Dong, *Coord. Chem. Rev.*, 2023, **491**, 215245.

9 X. Song, H. Huang, L. Xia, W. Jia, S. Yang, C. Wang and Y. Chen, *Adv. Sci.*, 2023, 2301279.

10 Z. Li, C. Wang, C. Dai, R. Hu, L. Ding, W. Feng, H. Huang, Y. Wang, J. Bai and Y. Chen, *Biomaterials*, 2022, **287**, 121668.

11 H. Yu, Y. Cheng, C. Wen, Y.-Q. Sun and X.-B. Yin, *Biomaterials*, 2022, **280**, 121308.

12 Y. Zhu, R. Zhao, L. Feng, C. Wang, S. Dong, M. V. Zyuzin, A. Timin, N. Hu, B. Liu and P. Yang, *ACS Nano*, 2023, **17**, 6833–6848.

13 C. Zhang, W.-J. Qin, X.-F. Bai and X.-Z. Zhang, *Nano Today*, 2020, **35**, 100960.

14 C. Liao, X. Liu, C. Zhang and Q. Zhang, *Semin. Cancer Biol.*, 2023, **88**, 172–186.

15 S. Wang, Z. Wang, Z. Li, J. Xu, X. Meng, Z. Zhao and Y. Hou, *Adv. Healthc. Mater.*, 2022, **11**, e2201240.

16 S. L. Li, P. Jiang, F. L. Jiang and Y. Liu, *Adv. Funct. Mater.*, 2021, **31**, 2100243.

17 Y. Rao, T. Fan, L. Zhou, K. Fang, Y. Sun, X. Hu, A. Wang, R. Li, Z. Zhu and C. Dong, *J. Controlled Release*, 2023, **354**, 701–712.

18 Y. He, S. Guo, Y. Zhang, Y. Liu and H. Ju, *Biomaterials*, 2021, **275**, 120962.

19 C. Zhang, J. Huang, X. Guo, X. Da, Z. Dai, M. Hassan, Y. Yu, X. Wang and Q. Zhou, *Nano Today*, 2023, **50**, 101824.

20 P. Lin, J. Shi, L. Ming, Y. Sheng, L. Song, M. Hong and Y. Zhang, *Chem. Eng. J.*, 2022, **442**, 135638.

21 Q. Yu, J. Zhou, J. Song, H. Zhou, B. Kang, H. Y. Chen and J. J. Xu, *Small*, 2023, **19**, 2206592.

22 M. Yuan, S. Liang, Y. Zhou, X. Xiao, B. Liu, C. Yang, P. a. Ma, Z. Cheng and J. Lin, *Nano Lett.*, 2021, **21**, 6042–6050.

23 S. Y. Wu, Y. X. Ye, Q. Zhang, Q. J. Kang, Z. M. Xu, S. Z. Ren, F. Lin, Y. T. Duan, H. J. Xu, Z. Y. Hu, S. S. Yang, H. L. Zhu, M. J. Zou and Z. C. Wang, *Adv. Sci.*, 2023, **10**, e2203742.

24 R. Li, Z. Lin, Q. Zhang, Y. Zhang, Y. Liu, Y. Lyu, X. Li, C. Zhou, G. Wu, N. Ao and L. Li, *ACS Appl. Mater. Interfaces*, 2020, **12**, 17936–17948.

25 R. Li, Z. Lin, Q. Zhang, Y. Zhang, Y. Liu, Y. Lyu, X. Li, C. Zhou, G. Wu and N. Ao, *ACS Appl. Mater. Interfaces*, 2020, **12**, 17936–17948.

26 Z. Zhang, R. Wang, X. Huang, R. Luo, J. Xue, J. Gao, W. Liu, F. Liu, F. Feng and W. Qu, *ACS Appl. Mater. Interfaces*, 2020, **12**, 5680–5694.

27 Q. Zhang, W. Lai, T. Yin, C. Zhang, C. Yue, J. Cheng, K. Wang, Y. Yang, D. Cui and W. J. Parak, *Bioconjugate Chem.*, 2018, **29**, 2120–2125.

28 Q. Zhang, T. Yin, G. Gao, J. G. Shapter, W. Lai, P. Huang, W. Qi, J. Song and D. Cui, *ACS Appl. Mater. Interfaces*, 2017, **9**, 17777–17785.

29 Y. Matsumura and H. Maeda, *Cancer Res.*, 1986, **46**, 6387–6392.

30 H. Maeda, T. Sawa and T. Konno, *J. Controlled Release*, 2001, **74**, 47–61.

31 X. Huang, B. Sheng, H. Tian, Q. Chen, Y. Yang, B. Bui, J. Pi, H. Cai, S. Chen and J. Zhang, *Acta Pharm. Sin. B*, 2023, **13**, 1303–1317.

32 W. Yang, C. Deng, X. Shi, Y. Xu, C. Dai, H. Wang, K. Bian, T. Cui and B. Zhang, *ACS Nano*, 2023, **17**, 4009–4022.

33 Y. Wang, D. Wang, Y. Zhang, H. Xu, L. Shen, J. Cheng, X. Xu, H. Tan, X. Chen and J. Li, *Bioact. Mater.*, 2023, **22**, 239–253.

34 J. Li, H. Tian, F. Zhu, S. Jiang, M. He, Y. Li, Q. Luo, W. Sun, X. Liu and P. Wang, *Adv. Healthcare Mater.*, 2022, **11**, 2201986.

35 M. Tang, Y. Shi, Y. Lu, J. Li, Z. Zhang, J. Ni, W. Wang, Y. Zhang, T. Sun and Z. Wu, *Chem. Eng. J.*, 2022, **449**, 137847.

36 S. Gao, H. Lin, H. Zhang, H. Yao, Y. Chen and J. Shi, *Adv. Sci.*, 2019, **6**, 1801733.

37 L. H. Liu, Y. H. Zhang, W. X. Qiu, L. Zhang, F. Gao, B. Li, L. Xu, J. X. Fan, Z. H. Li and X. Z. Zhang, *Small*, 2017, **13**, 1701621.

38 C. P. Liu, T. H. Wu, C. Y. Liu, K. C. Chen, Y. X. Chen, G. S. Chen and S. Y. Lin, *Small*, 2017, **13**, 1700278.

39 Z. Zhang, R. Wang, X. Huang, R. Luo, J. Xue, J. Gao, W. Liu, F. Liu, F. Feng and W. Qu, *ACS Appl. Mater. Interfaces*, 2020, **12**, 5680–5694.

40 Q. You, Q. Sun, M. Yu, J. Wang, S. Wang, L. Liu, Y. Cheng, Y. Wang, Y. Song, F. Tan and N. Li, *ACS Appl. Mater. Interfaces*, 2017, **9**, 40017–40030.

41 Y. Ma, Z. Su, L. Zhou, L. He, Z. Hou, J. Zou, Y. Cai, D. Chang, J. Xie, C. Zhu, W. Fan, X. Chen and S. Ju, *Adv. Mater.*, 2022, **34**, e2107560.

42 T. Yin, H. Chen, A. Ma, H. Pan, Z. Chen, X. Tang, G. Huang, J. Liao, B. Zhang, M. Zheng and L. Cai, *Biomaterials*, 2023, **293**, 121992.

43 S. Wilhelm, A. J. Tavares, Q. Dai, S. Ohta, J. Audet, H. F. Dvorak and W. C. W. Chan, *Nat. Rev. Mater.*, 2016, **1**, 16014.

44 B. Ouyang, W. Poon, Y. N. Zhang, Z. P. Lin, B. R. Kingston, A. J. Tavares, Y. Zhang, J. Chen, M. S. Valic, A. M. Syed, P. MacMillan, J. Couture-Senécal, G. Zheng and W. C. W. Chan, *Nat. Mater.*, 2020, **19**, 1362–1371.

45 Y. Matsumoto, J. W. Nichols, K. Toh, T. Nomoto, H. Cabral, Y. Miura, R. J. Christie, N. Yamada, T. Ogura, M. R. Kano, Y. Matsumura, N. Nishiyama, T. Yamasoba, Y. H. Bae and K. Kataoka, *Nat. Nanotechnol.*, 2016, **11**, 533–538.